Negative Linear Compressibility in Organic-Inorganic Hybrid Perovskite $[NH_2NH_3]X(HCOO)_3$ (X=Mn, Fe, Co)

P.S. Ghosh[*,†] and I. Ponomareva[†]

†*Department of Physics, University of South Florida, Tampa, Florida 33620, USA*

‡*Glass & Advanced Materials Division, Bhabha Atomic Research Centre, Mumbai 400 085, India*

E-mail: psghosh@mail.usf.edu

Abstract

Hybrid organic-inorganic perovskite $[NH_2NH_3][X(HCOO)_3]$ (X=Mn, Fe, Co) have a so-called "wine-rack" type of geometry that could give origin to the rare property of negative linear compressibility, which is an exotic and highly desirable material response. We use first-principles density functional theory computations to probe the response of these materials to hydrostatic pressure and predict that indeed all three of them exhibit negative linear compressibility above a critical pressure of 1 GPa. Calculations reveal that under pressure XO_6 octahedra and -HCOO ligands remain relatively rigid while XO_6 octahedra tilt significantly which leads to highly anisotropic mechanical properties and expansion along certain directions. These trends are common for the three materials considered.

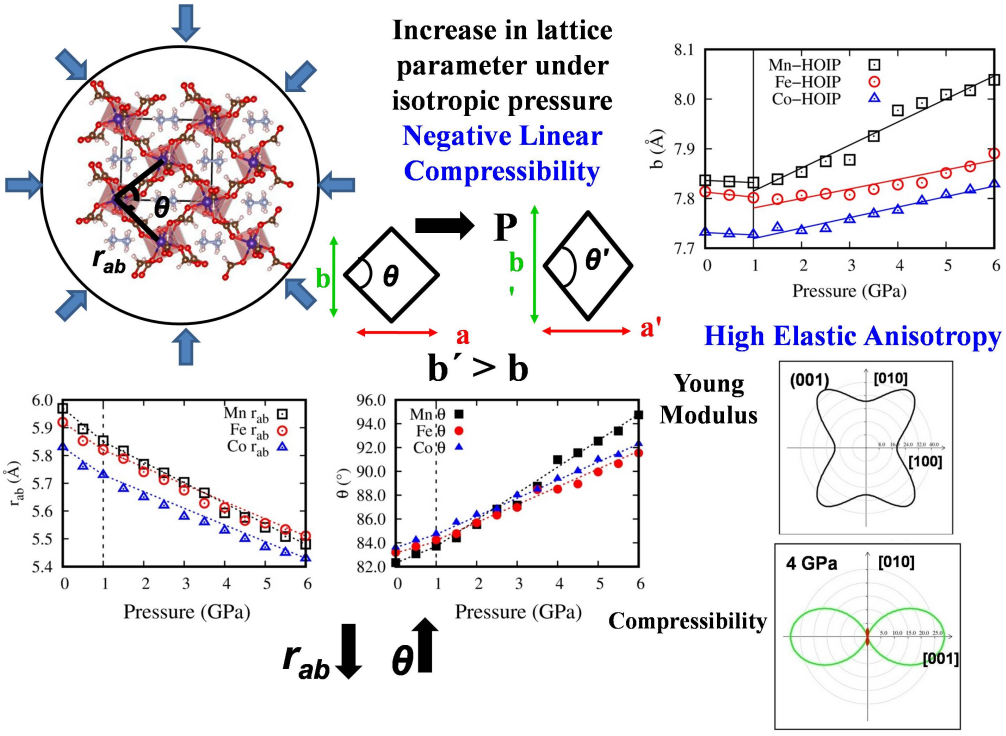

Formate family of hybrid organic-inorganic perovskites (HOIP), $AX(HCOO)_3$, is a large family with rich and diverse properties. Due to the structural flexibility and chemical diversity, "A" and "X" sites could be occupied by organic amine cations (A=dimethylammonium,

ammonium, hydraginium, guanidinium, or formamidinium, etc.) and six-coordinated divalent metals (or mixed monovalent and trivalent metals), respectively.[1,2] Many intriguing and diverse properties like, magnetism, ferroelectricity, magnetoelectricity, multiferroicity, negative thermal expansion have been found in formate perovskites.[2–9,9–12] Recently, a rare property of negative linear compressibility (NLC) has been predicted from first-principles simulations in $[NH_2NH_3][Co(HCOO)_3]$.[13] NLC is associated with expansion along a certain direction as the volume reduces in response to hydrostatic pressure. This counterintuitive response is not just of academic curiosity but could be used in a variety of practical applications, e.g., high-pressure deep-sea optical devices, ultra-sensitive pressure detectors for sonar and aircraft height readings, artificial muscles, actuators, and next-generation body armor with great shock resistance,[14,15] just to name a few.

In the recent years the number of hybrid organic-inorganic materials that exhibit NLC has grown.[14,15] The hinging-type lattice distortions under compression leading to NLC have been reported for metal-organic framework materials $[NH_4]Zn(HCOO)_3$,[16] [Ag(ethylenediamine)]NO_3,[17] MFM-133(M) (M=Zr,Hf),[18] $Cu(4,4'\text{-bpy})_2(H_2O)_2]\cdot SiF_6$[19] *etc.* A similar mechanism of NLC has been revealed in topologically different structures of organo-metallic complexes [Fe(dpp)2(NCS)2].py (dpp=dipyrido[3,2-a:2',3'-c]phenazine, py=pyridine),[20] $[(C_6F_5Au)_2(\mu\text{-}1,4\text{-diisocyanobenzene})]$,[21] $Co(SCN)_2(pyrazine)_2$[22] and pure organic systems like, methanol monohydrate (MM),[23] ammonium oxalate monohydrate (AOM).[24] One outstanding example is linear di-gold complex $[(C_6F_5Au)_2(\mu\text{-}1,4\text{-diisocyanobenzene})]$ which undergoes substantial negative linear compression (-13 TPa^{-1}) over the pressure range from ambient to 4.39 GPa. In molecular complexes, the largest NLC effect has been reported by Shepherd et al. in the spin crossover complex [Fe(dpp)2(NCS)2].py.[20]

The prediction of NLC in $[NH_2NH_3][Co(HCOO)_3]$[13] (Co-HOIP) is attractive as the phase associated with such property exist near room temperature and, therefore, is valuable for practical applications. More precisely, Co-HOIP undergoes phase transition from *Pnma* to $Pna2_1$ phase around 343 K.[25] It was shown computationally that NLC in $Pna2_1$ phase of

Co-HOIP originates from its special geometry that can be described as "wine-rack" type.[26] The wine-rack is composed of relatively rigid units "struts" (-HCOO ligands and CoO_6 octahedra) connected via relatively soft "hinges" (tilts of CoO_6 octahedra). Under pressure the hinge angle could increase causing expansion along the direction subtended by it. This mechanism is expected to activate in materials with highly anisotropic mechanical properties. The aims of this study are (i) to predict that the NLC occurs in some other members of $[NH_3NH_2]X(HCOO)_3$ (X=Mn,Fe,Co) formate family, (ii) report variation of NLC with X cation; (iii) report the response of this family to the hydrostatic pressure.

We carry out computations using spin-polarized density functional theory as implemented in the Vienna Ab-initio Simulation Package (VASP).[27,28] The exchange-correlation energies are computed using the generalized gradient approximation (GGA) with the Perdew-Burke-Ernzerhof (PBE) parameterization.[29] The zero-damping DFT-D3 approach of Grimme *et al.*[30] is used to incorporate the van der Waals interactions into the GGA. The ion-electron interactions are modeled with the projected augmented wave (PAW) potentials[31] from VASP psedopotential library. The PAW potentials of Mn, Fe, Co, C, N, O, and H include valence electrons as $p^6d^6s^1$, d^7s^1, d^8s^1, s^2p^2, s^2p^3, s^2p^4 and s^1, respectively. We used 700 eV energy cutoff for plane wave basis expansion. For the Brillouin zone integration, a Monkhorst-Pack[32] k-space mesh of 5×5×3 in reciprocal space is utilized. With these choices of k-mesh and energy cutoff a energy convergence of 4 meV/unit cell with respect to is achieved. In other words, calculation performed with higher energy cutoff and denser k-mesh will give deviation in energy within 4 meV/unit cell. The Hubbard correction as proposed by Dudarev *et al.*[33] is introduced to account for the Coulomb repulsion between localized d-electrons of transition metals. The U_{eff} value of 2.0 eV for Co-d,[34,35] 4.0 eV for Fe-d and Mn-d is chosen based on previous DFT calculations on oxides and photo-emission spectroscopy data.[36–38] The conjugate gradient approach is used to compute full structural optimization until residual forces on ions are less than 0.1 meV/Å. The linear compressibilities, Young's moduli, and Poisson ratios are determined from single crystal elastic constants computed using the finite

difference method[39] as implemented in the VASP package, and then analyzed using ElAM software.[40]

The low temperature polar $Pna2_1$ phase of $[NH_2NH_3]X(HCOO)_3$ with X= Mn, Fe, Co transform to non-polar phase $Pnma$ at 355 K,[8] 347 K[41] and 353 K,[25] respectively. In $[NH_2NH_3]Mn(HCOO)_3$ (Mn-HOIP) and $[NH_2NH_3][Co(HCOO)_3]$(Co-HOIP) low temperature phase was predicted to be ferroelectric.[8,42] In the literature no information is available regarding ferroelectricity in $[NH_2NH_3]Fe(HCOO)_3$ (Fe-HOIP). At high temperature, $NH_2NH_3^{+1}$ molecules exhibit dynamical disorder leading to paraelectric phase. In order to obtain ground state structure, experimentally reported low temperature structure is subjected to full structural relaxation using GGA+U+D3 approach in the ferromagnetic (FM), A-type anti-ferromagnetic (A-AFM), C-type AFM (C-AFM) and G-type AFM (G-AFM) configurations. Our data are presented in Table 1 where we also provide experimental data from the literature. The comparison reveals excellent agreement with experiment for the lattice parameters and volume. We note the decrease of the unit cell volume from 817.6, 788.2 to 766.0 $Å^3$ in Mn-HOIP, Fe-HOIP and Co-HOIP, respectively, which could be attributed to the decrease in ionic radius on going from Mn^{2+}, Fe^{2+} to Co^{2+}. For Mn-HOIP and Co-HOIP, we find G-AFM ordering to be most stable, while for Fe-HOIP it is the FM ordering that is the most favorable. However, the energy difference between different magnetic configurations is rather small suggesting low temperature for the onset of magnetic ordering. Indeed, experimentally AFM ordering with Neel temperature 7.9 and 13.9 K has been reported for Mn- and Co-HOIP,[8] respectively, while FM ordering has been reported for Fe-HOIP below 12.5 K.[41]

To predict structural evolution of HOIP's in the presence of isotropic pressure, the ground state structures are subjected to full structural relaxations under the isotropic pressure in the 0-6 GPa range. Such simulations model application of hydrostatic pressure at low temperatures and were found to provide good agreement with experiment for TMCM-$CdCl_3$ (TMCM = tri-methyl chloro-methyl ammonium).[43] For each pressure the space groups of

Table 1: The lattice parameters, volumes, magnetic moments and relative cohesive energies in Mn-HOIP, Fe-HOIP, Co-HOIP obtained in computations. The experimental values from the literature are provided for comparison.

Sp. Gr. ($Pna2_1$)	a, b, c (Å)	V_0 (Å^3/u.c.)	M_B (μ_B)	ΔE (meV/u.c.)
Mn-HOIP				
FM	8.94, 7.83, 11.68	817.5	4.7	10
C-AFM	8.94, 7.83, 11.68	817.8	4.7	3
A-AFM	8.95, 7.83, 11.67	818.5	4.7	6
G-AFM	8.94, 7.83, 11.67	817.6	4.7	0
Experiment[8]	8.93, 7.82, 11.69	816.6	(at 110 K)	
Fe-HOIP				
FM	8.80, 7.81, 11.46	788.2	3.8	0
A-AFM	8.79, 7.82, 11.46	788.0	3.8	16
C-AFM	8.79, 7.82, 11.46	787.9	3.8	12
G-AFM	8.79, 7.82, 11.46	787.9	3.8	6
Experiment[41]	8.81, 7.78, 11.66	799.3	(at 290 K)	
Co-HOIP				
FM	8.65, 7.73, 11.45	766.4	2.7	16
C-AFM	8.64, 7.73, 11.46	766.1	2.7	15
A-AFM	8.64, 7.73, 11.46	766.2	2.7	28
G-AFM	8.65, 7.73, 11.46	766.0	2.7	0
Experiment[25]	8.65, 7.73, 11.49	767.9	(at 100 K)	

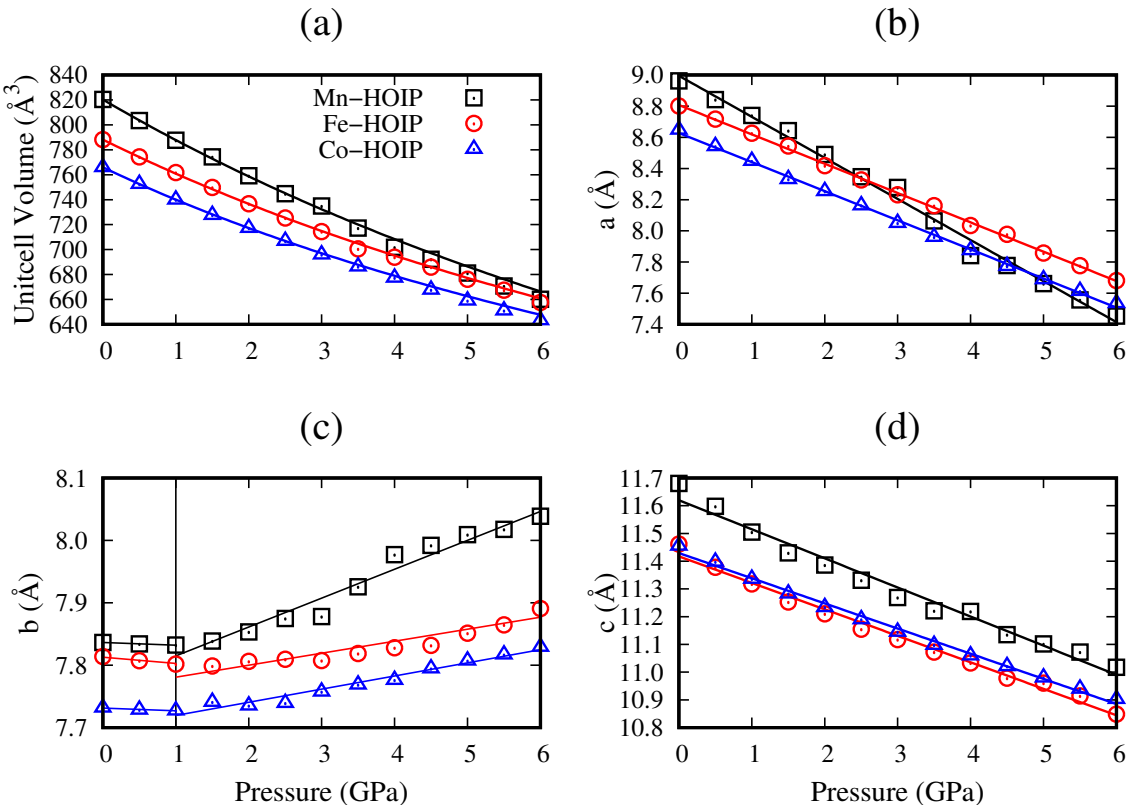

Figure 1: Variation of the unitcell volume, V, (a) and lattice parameters (b), (c) and (d) as a function of pressure in Mn-, Fe- and Co-HOIP. The solid lines give fit to Birch–Murnaghan equation of state in (a) and to linear dependence in (b), (c) and (d). The data for Co-HOIP is taken from our previous study[13] for comparison.

the fully relaxed structures are analysed using ISOTROPY[44] with the default tolerance of 10^{-5} and 10^{-3} for lattice parameters and atomic positions, respectively. We find that the structures remain in the $Pna2_1$ space group for each pressure investigated. We have also reduced the tolerance to 10^{-3} and 10^{-1} and found that the space group remains $Pna2_1$. Thus, our calculations predict no structural phase transitions in the pressure range considered in this study. Figure 1 reports evolution of the unit cell volume and lattice parameters of HOIPs as a function of pressure. Fitting pressure-volume data to 3^{rd} order Birch–Murnaghan equation of state yields bulk modulus B_0= 25.1, 27.5 and 27.9 GPa for Mn-HOIP, Fe-HOIP and Co-HOIP, respectively, which are in agreement to the range of bulk moduli 25.7-31.0 GPa measured for $[C(NH_2)_3]$-M-$(HCOO)_3$ (M=Cd,Co)[45,46] (Table 2). It is interesting to note that B_0 of HOIP with -HCOO group is higher than other organometallic complexes and

even higher than inorganic salt NaCl (B_0=24 GPa).[47]

Under pressure the a- and c-lattice parameters decrease exhibiting the usual positive linear compressibility (PLC). However, the behavior of b-lattice parameter is quite different. While below 1.0 GPa the b-lattice parameter decreases in response to pressure as well, above 1.0 GPa the trend reverses and all three materials exhibit NLC. To compute linear compressibility, $K_L = -\frac{1}{L}(\frac{dL}{dP})_T$, for b-lattice parameter we fit computational data with linear dependence in both low and high pressure region (see Fig 1). These K_a, K_b and K_c values are presented in Table 2, where they are also compared with the ones for the same material family and some other organic and organometallic complexes. We find very good agreement between our DFT predictions and experimental data for the formate family of Cu-GF (in $Pna2_1$ Sp. Gr, GF=Guanidinium formate), Mn-GF and Co-GF (in $Pnna$ Sp. Gr.), and NH_4-$Zn(HCOO)_3$ (in $P6_322$ Sp. Gr.). Among NH_2NH_3-$X(HCOO)_3$ materials all three compressibilities are comparable, while the largest in magnitude NLC is predicted for Mn-HOIP. Our predicted K_a and K_c values also compare well with other members of formate family, as well as AOM and MM. However, the negative K_b values are smaller in magnitude than the best ones reported in the literature. Interestingly, in the low pressure range of 0-1 GPa NH_2NH_3-$Mn(HCOO)_3$ and NH_2NH_3-$Co(HCOO)_3$ exhibit positive compressibility, which is smaller than the the one for diamond (0.75 TPa^{-1}). Such materials are characterized as zero linear compressibility materials, which is another highly desirable property.[48,49]

In order to confirm that our prediction of NLC is independent of choice of exchange-correlation functional and magnetic configuration of transition metals, structural optimizations are again performed with Hubbard corrected local density approximations (LDA+U)[51] with FM, A-AFM, C-AFM and G-AFM configurations. For Fe-HOIP, LDA+U predicts FM configuration as ground state and lattice parameters and volume underestimates experimental values by 4.5% and 9.6%, respectively. The pressure-volume data is fitted to the third order Birch–Murnaghan equation of state which give B_0=27.3 GPa and it is only 1.0% lower compared to our GGA+U+D3 calculated value. The LDA+U predicts both PLC and

Table 2: Linear compressibility of the lattice parameters (K_a, K_b, K_c), struts ($K_{r_{ab}}$), hinges (K_θ) in TPa^{-1} and bulk modulus (B_0 in GPa) of HOIP's, compared with experimental values of the materials in the same family and other materials showing NLC.

system	Pressure range (GPa)	K_a	K_b	K_c	$K_{r_{ab}}$	K_{r_c}	K_θ	B_0
NH_2NH_3-$Mn(HCOO)_3$	0-1	24.7	0.5	15.0	20.1	9.2	-17.0	25.1
	1-6	24.7	-6.0	15.0	12.9	9.2	-23.4	25.1
NH_2NH_3-$Fe(HCOO)_3$	0-1	21.7	1.3	8.5	11.9	9.0	-11.1	27.5
	1-6	21.7	-2.5	8.5	11.3	9.0	-16.4	27.5
NH_2NH_3-$Co(HCOO)_3$	0-1	21.6	0.6	7.9	14.1	6.8	-13.1	27.9
	1-6	21.6	-2.7	7.9	9.2	6.8	-15.2	27.9
$C(NH_2)_3$-$Mn(HCOO)_3$	0.00-1.12[45]	26.6	15.4	0.11	16.2	12.4	17.7	
$C(NH_2)_3$-$Co(HCOO)_3$	0.00-1.19[45]	20.7	12.5	0.96	11.4	10.1	13.2	
$C(NH_2)_3$-$Zn(HCOO)_3$	0.00-0.66[50]	18.3	3.6	8.4				
$C(NH_2)_3$-$Cu(HCOO)_3$	0.00-0.66[50]	28.7	4.0	11.9				
NH_4-$Zn(HCOO)_3$	0.00-0.93[16]	15.8	-	-1.8				32.8
$Fe(dpp)_2(NCS)_2$.py	0.00-2.48[20]	-10.0	12.0	53.0				12.9
$(C_6F_5Au)_2$(m-1,4-DSB)	0.00-2.42[21]	-12.6	29.0	31.3				7.5
AOM	5.10-11.50[24]		-2.3					38.7
MM	0.00-0.50[23]	-2.7	31.9	108.0				3.8

NLC in b-lattice parameters with K_b=2.9 TPa^{-1} (in 0-2 GPa range) and -2.1 TPa^{-1} (in 2-6 GPa range), respectively. Similarly, for Mn-HOIP, LDA+U predicts G-AFM as ground state and lattice parameters and volume underestimates experimental values by 3.0% and 7.7%, respectively. The LDA+U calculated B_0 (=24.3 GPa) is 3.2% lower compared to our GGA+U+D3 calculated value. Still LDA+U calculated B_0 is in close agreement with experimental values for other formate family member.[45,46] The LDA+U predicts both PLC and NLC in b-lattice parameters with K_b=0.7 TPa^{-1} (in 0-1 GPa range) and -3.9 TPa^{-1} (in 1-6 GPa range), respectively. We found that prediction of NLC remains valid with LDA+U, however, there exist quantitative differences in predictions, for example, the pressure at which the NLC effect onsets. Further, structural optimizations under hydrostatic pressure using GGA+U+D3 for FM, A-AFM and C-AFM confirms the NLC effect persist for all the magnetic configurations considered in the study.

The structures of the HOIP can be categorized in "wine-rack" type[26] in which origin of

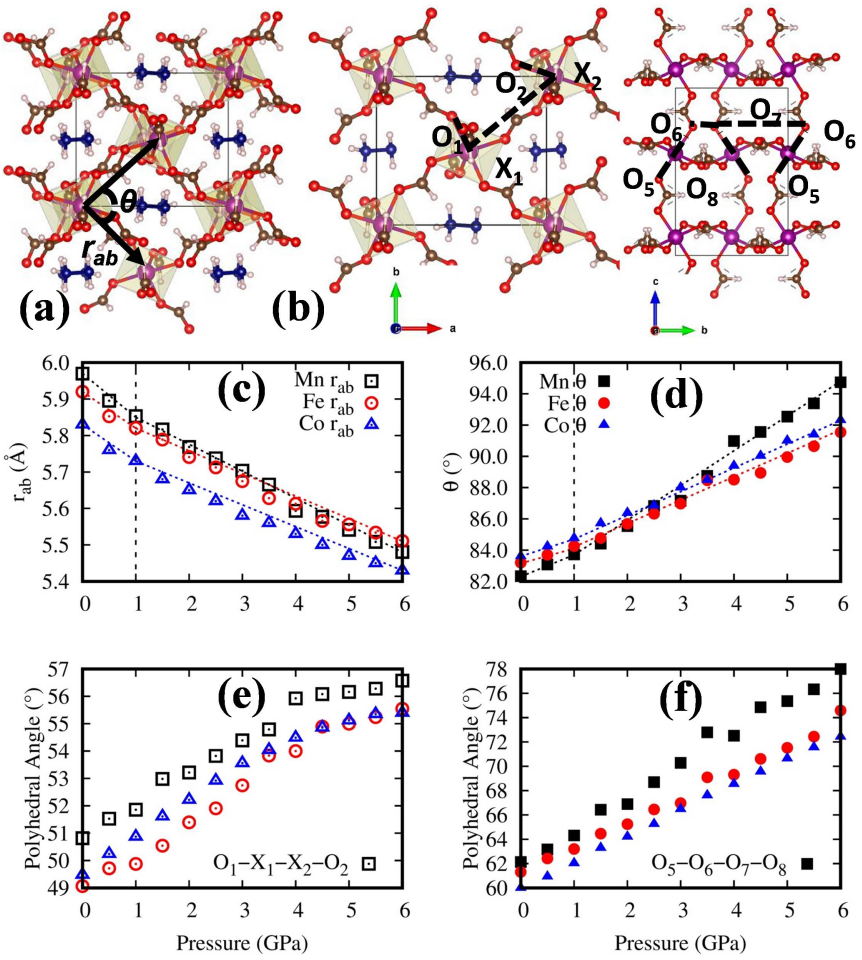

Figure 2: (a) Structure of $[NH_2NH_3]X(HCOO)_3$ (X=Mn,Fe,Co), shown in different planes to indicate angles and distances (a)-(b). Color scheme: X^{2+}, purple; O, red; C, brown; N, blue; H, gray. Dependence of strut length (c) and hinge angle (d) and dihedral angles (e)-(f) on pressure. Dotted lines show fitting values of $K_{r_{ab}}$ and K_θ in 0-1 and 1-6 GPa pressure range.

NLC can be described by the strut-hinge mechanism.[45] The struts and hinges are marked by r_{ab} and θ, respectively, in Fig. 2(a). Recently, Cheetham et al.[16] have shown that NLC in Zn-formate originated from the pressure evolution of struts lengths and hinge angles. More precisely, under pressure the strut length decreases while the hinge angle increases. If the latter one overpowers the former one the NLC occurs. Same mechanism was predicted in $[NH_2NH_3][Co(HCOO)_3]$.[13] To test whether this mechanism is universal to $NH_2NH_3X(HCOO)_3$ (X=Mn, Fe, Co) we computed the pressure evolution for both r_{ab} and θ and report it in Fig 2(c). The data confirm that for all materials in the family the strut

Table 3: Single crystal elastic constants C_{ij} (in GPa) and linear compressibilities K (in TPa^{-1}) along crystallographic axes computed at different pressures.

	C_{11}	C_{12}	C_{13}	C_{22}	C_{23}	C_{33}	C_{44}	C_{55}	C_{66}	$K(100)$	$K(010)$	$K(001)$
Mn-HOIP												
0 GPa	34.0	28.6	13.1	54.7	20.4	46.7	11.5	9.8	16.6	23.1	0.7	14.4
4 GPa	32.3	33.0	23.9	88.2	42.9	61.8	6.4	13.3	15.2	28.6	-2.8	7.0
Fe-HOIP												
0 GPa	29.9	26.1	14.4	56.2	22.2	49.7	8.8	7.0	14.6	27.4	0.3	11.9
4 GPa	28.7	29.9	27.9	72.1	35.2	52.6	7.7	11.5	13.7	34.8	-1.2	1.7
Co-HOIP[13]												
0 GPa	33.8	29.7	15.3	62.3	23.3	57.6	9.7	8.8	16.8	24.4	0.4	11.0
4 GPa	37.5	39.6	23.0	85.1	37.2	68.3	9.9	15.1	13.3	25.6	-3.7	7.8

length decreases, while the hinge angle increases in response to pressure. Interestingly, even the slopes of the dependence are comparable between the materials. To quantify the relative strength of these evolution we compute linear compressibilities of K_θ, $K_{r_{ab}}$ and their ratio $|K_\theta|/K_{r_{ab}}$. The compressibilities, K_θ and $K_{r_{ab}}$, are reported in 0-1 and 1-6 GPa pressure range (Table 2). In 0-1 GPa range, the ratios are 0.8, 0.9 and 0.9, respectively, for Mn-, Fe- and Co-HOIP. Similarly, in the 1-6 GPa range those ratios are 2.5, 1.8 and 1.7 for Mn-, Fe- and Co-HOIP, respectively, which confirms that the increase in the hinge angle indeed overpowers the decrease in the strut length giving origin to NLC in 1-6 GPa range. Interestingly, the rate of change of hinge angle is highest in Mn-HOIP leading to largest value of NLC in this family of HOIP. On the contrary, decrease in strut length overpowers increase in hinge angle in 0-1 GPa range leading to PLC of K_b.

It was demonstrated in Ref[13] that in Co-HOIP such unusual behavior can be traced to the rigidity of the molecular blocks which causes them to tilt in response to deformations. To confirm that this is still the case for the other HOIPs considered here we computed C-O bond lengths, O-C-O bond angles and oxygen octhedra tilts. We found no change in the C-O bond length or O-C-O bond angles in the formate ligand, which demonstrates the stiffness of the ligand due to strong covalent bonding in all these HOIP. The X-O bond (X=Mn, Fe, Co) decreases by up to 1.8, 2.8 and 2.5% in the XO_6 unit. These allows to confirm that

indeed the individual units are stiff under pressure. Octahedra tilts can be quantified by the dihedral angles as shown in Fig. 2(b). Figure 2(e)-(f) present the pressure evolution of these angles, which reveals considerable tilts (up to 26%) that occur to accommodate pressure. The change in the tilt angle O_1-X_1-X_2-O_2, produces a 9°, 11° and 7° change in the X-O-C angle, respectively for X=Mn, Fe and Co, causing r_{ab} to decrease while θ to increase. Therefore, our data validate the rigid strut and flexible hinge mechanism for NLC in these HOIPs which originates from tilting of rigid units.

This atomistic mechanism in turn would manifest in the anisotropy of mechanical properties[26] which can be quantified by their directional dependence. Figure 3 presents directional maps for Young modulus, Poisson's ratio and compressibility of Mn-HOIP, Fe-HOIP and Co-HOIP which were computed using ElAM[40] from the elastic constants obtained from DFT listed in Table 3. The maps show that similar to the case of Co-HOIP[13] the mechanical response of Mn-HOIP and Fe-HOIP is highly anisotropic, with [001] being the hardest direction and [110] being the second hardest. These are the directions of XO_6 chains and formate ligands (-HCOO), respectively, as shown in Fig. 2(a). Figure 3(b) shows a map of Poisson's ratios, which exhibits high anisotropy in materials response to uniaxial deformation. We have followed the approach of Ref[13] and computed compressibility using the equation $K_i = \sum_{j=1,3} S_{iijj}$, where S_{iijj} are components of the elastic compliance tensor and i and j represent primary axes. The advantage of this approach is that it allows to accurately compute compressibility at different pressures. Table 3 and Fig. 3(c) present our data which confirm that at zero pressure the compressibility is positive, while at high pressure of 4 GPa the compressibility becomes negative. From the compressibility maps (Fig.3(c)) we can also see that the largest in magnitude NLC is along b direction.

In summary, we used first-principles DFT simulations to predict NLC in the $[NH_2NH_3][X(HCOO)_3]$ (X=Mn, Fe, Co) family in the space group $Pna2_1$. As Mn-HOIP, Fe-HOIP, and Co-HOIP undergoes phase transition into $Pna2_1$ phase from $Pnma$ at 355 K,[8] 347 K[41] and 353 K,[25] respectively, we expect NLC to occur in the wide temperature range below the phase transi-

tion temperature, which is valuable for practical applications. The calculations predict that under pressure -HCOO and XO_6 units remain rigid while XO_6 exhibits large tilts. These atomistic mechanisms give origin to highly anisotropic mechanical response and NLC which can be well described by the strut-hinge model. The response of the struts and hinges to hydrostatic pressure is quantified by their linear compressibility, whose ratio predicts the relative strength of the two. Below the critical pressure of 1 GPa the ratio is less than one indicating that struts shrink faster than the hinge angle increase. Above this critical pressure the ratio becomes greater than one signifying that hinge angle increase overpowers strut compression, which gives origin to NLC. We find that the response of the three HOIPs to the pressure is very similar, suggesting that the entire family of these materials is likely to exhibit the exotic NLC. Out of the three HOIPs, Mn-HOIP was found to have NLC largest in magnitude.

The work is supported by the National Science Foundation under the grant EPMD-2029800.

References

(1) Li, W.; Wang, Z.; Deschler, F.; Gao, S.; Friend, R. H.; Cheetham, A. K. Chemically diverse and multifunctional hybrid organic-inorganic perovskites. *Nat. Rev. Mater.* **2017**, *2*, 16099.

(2) Ma, Y.; Sun, Y. Multiferroic and thermal expansion properties of metal-organic frameworks. *J. Appl. Phy.* **2020**, *127*, 080901.

(3) Zhang, W.; Xiong, R.-G. Ferroelectric Metal-Organic Frameworks. *Chem. Rev.* **2012**, *112*, 1163–1195, PMID: 21939288.

(4) Maczka, M.; Gagor, A.; Ptak, M.; Paraguassu, W.; da Silva, T. A.; Sieradzki, A.;

Pikul, A. Phase Transitions and Coexistence of Magnetic and Electric Orders in the Methylhydrazinium Metal Formate Frameworks. *Chem. Mater.* **2017**, *29*, 2264–2275.

(5) Ma, Y.; Wang, Y.; Cong, J.; Sun, Y. Magnetic-Field Tuning of Hydrogen Bond Order-Disorder Transition in Metal-Organic Frameworks. *Phys. Rev. Lett.* **2019**, *122*, 255701.

(6) Gomez-Aguirre, L. C.; Pato-Doldan, B.; Mira, J.; Castro-Garcia, S.; Senaris-Rodriguez, M. A.; Sanchez-Andujar, M.; Singleton, J.; Zapf, V. S. Magnetic Ordering-Induced Multiferroic Behavior in $[CH_3NH_3][Co(HCOO)_3]$ Metal-Organic Framework. *J. Am. Chem. Soc.* **2016**, *138*, 1122–1125.

(7) Szafranski, M.; Wei, W.-J.; Wang, Z.-M.; Li, W.; Katrusiak, A. Research Update: Tricritical point and large caloric effect in a hybrid organic-inorganic perovskite. *APL Mater.* **2018**, *6*, 100701.

(8) Chen, S.; Shang, R.; Hu, K.-L.; Wang, Z.-M.; Gao, S. *Inorg. Chem. Front.* **2014**, *1*, 83.

(9) Stroppa, A.; Jain, P.; Barone, P.; Marsman, M.; Perez-Mato, J. M.; Cheetham, A. K.; Kroto, H. W.; Picozzi, S. Electric Control of Magnetization and Interplay between Orbital Ordering and Ferroelectricity in a Multiferroic Metal–Organic Framework. *Angew. Chem. Int. Ed.* **2011**, *50*, 5847–5850.

(10) Di Sante, D.; Stroppa, A.; Jain, P.; Picozzi, S. Tuning the Ferroelectric Polarization in a Multiferroic Metal–Organic Framework. *J. Am. Chem. Soc.* **2013**, *135*, 18126–18130.

(11) Stroppa, A.; Barone, P.; Jain, P.; Perez-Mato, J. M.; Picozzi, S. Hybrid Improper Ferroelectricity in a Multiferroic and Magnetoelectric Metal-Organic Framework. *Adv. Mater.* **2013**, *25*, 2284–2290.

(12) Ghosh, S.; Di Sante, D.; Stroppa, A. Strain Tuning of Ferroelectric Polarization in Hybrid Organic Inorganic Perovskite Compounds. *J. Phys. Chem. Lett.* **2015**, *6*, 4553–4559.

(13) Ghosh, P. S.; Ponomareva, I. Negative Linear Compressibility in [NH3NH2]Co(HCOO)3 and Its Structural Origin Revealed from First Principles. *J. Phys. Chem. Lett.* **2021**, *12*, 7560–7565.

(14) Baughman, R. H.; Stafström, S.; Cui, C.; Dantas, S. O. Materials with Negative Compressibilities in One or More Dimensions. *Science* **1998**, *279*, 1522–1524.

(15) Goodwin, A. L.; Keen, D. A.; Tucker, M. G. Large negative linear compressibility of $Ag_3[Co(CN)_6]$. *Proceedings of the National Academy of Sciences* **2008**, *105*, 18708–18713.

(16) Li, W.; Probert, M. R.; Kosa, M.; Bennett, T. D.; Thirumurugan, A.; Burwood, R. P.; Parinello, M.; Howard, J. A. K.; Cheetham, A. K. Negative Linear Compressibility of a Metal-Organic Framework. *J. Am. Chem. Soc.* **2012**, *134*, 11940–11943.

(17) Cai, W.; Katrusiak, A. Giant negative linear compression positively coupled to massive thermal expansion in a metal-organic framework. *Nat. Commun.* **2014**, *5*, 4337.

(18) Yan, Y.; O'Connor, A. E.; Kanthasamy, G.; Atkinson, G.; Allan, D. R.; Blake, A. J.; Schroder, M. Unusual and Tunable Negative Linear Compressibility in the Metal-Organic Framework MFM-133(M) (M = Zr, Hf). *J. Am. Chem. Soc.* **2018**, *140*, 3952–3958.

(19) Chen, Z.; Xu, B.; Li, Q.; Meng, Y.; Quan, Z.; Zou, B. Selected Negative Linear Compressibilities in the Metal-Organic Framework of $[Cu(4,4'\text{-bpy})_2(H_2O)_2]\cdot SiF_6$. *Inorg. Chem.* **2020**, *59*, 1715–1722.

(20) Shepherd, H. J.; Palamarciuc, T.; Rosa, P.; Guionneau, P.; Molnar, G.; Letard, J.-F.; Bousseksou, A. Antagonism between Extreme Negative Linear Compression and Spin Crossover in $[Fe(dpp)_2(NCS)_2]$.py. *Angew. Chem. Int. Ed.* **2012**, *51*, 3910–3914.

(21) Woodall, C. H.; Beavers, C. M.; Christensen, J.; Hatcher, L. E.; Intissar, M.; Parlett, A.; Teat, S. J.; Reber, C.; Raithby, P. R. Hingeless Negative Linear Compression in the Mechanochromic Gold Complex [$(C_6F_5Au)_2$(μ-1,4-diisocyanobenzene)]. *Angew. Chem. Int. Ed.* **2013**, *52*, 9691–9694.

(22) Zeng, Q.; Wang, K.; Qiao, Y.; Li, X.; Zou, B. Negative Linear Compressibility Due to Layer Sliding in a Layered Metal-Organic Framework. *J. Phys. Chem. Lett.* **2017**, *8*, 1436–1441.

(23) Fortes, A. D.; Suard, E.; Knight, K. S. Negative Linear Compressibility and Massive Anisotropic Thermal Expansion in Methanol Monohydrate. *Science* **2011**, *331*, 742–746.

(24) Qiao, Y.; Wang, K.; Yuan, H.; Yang, K.; Zou, B. Negative Linear Compressibility in Organic Mineral Ammonium Oxalate Monohydrate with Hydrogen Bonding Wine-Rack Motifs. *J. Phys. Chem. Lett.* **2015**, *6*, 2755–2760.

(25) Gunatilleke, W. D. C. B.; Wei, K.; Niu, Z.; Wojtas, L.; Nolas, G.; Ma, S. Thermal conductivity of a perovskite-type metal-organic framework crystal. *Dalton Trans.* **2017**, *46*, 13342–13344.

(26) Cairns, A. B.; Goodwin, A. L. Negative linear compressibility. *Phys. Chem. Chem. Phys.* **2015**, *17*, 20449–20465.

(27) Kresse, G.; Hafner, J. Ab initio molecular dynamics for liquid metals. *Phys. Rev. B* **1993**, *47*, 558–561.

(28) Kresse, G.; Furthmuller, J. Efficiency of ab-initio total energy calculations for metals and semiconductors using a plane-wave basis set. *Comput. Mater. Sci.* **1996**, *6*, 15 – 50.

(29) Perdew, J. P.; Burke, K.; Ernzerhof, M. Generalized Gradient Approximation Made Simple. *Phys. Rev. Lett.* **1996**, *77*, 3865–3868.

(30) Grimme, S.; Antony, J.; Ehrlich, S.; Krieg, H. A consistent and accurate ab initio parametrization of density functional dispersion correction (DFT-D) for the 94 elements H-Pu. *J. Chem. Phys.* **2010**, *132*, 154104.

(31) Blöchl, P. E. Projector augmented-wave method. *Phys. Rev. B* **1994**, *50*, 17953–17979.

(32) Monkhorst, H. J.; Pack, J. D. Special points for Brillouin-zone integrations. *Phys. Rev. B: Condens. Mater. Phys.* **1976**, *13*, 5188.

(33) Dudarev, S.; Botton, G.; Savrasov, S.; Humphreys, C.; Sutton, A. Electron-energy-loss spectra and the structural stability of nickel oxide: An LSDA+U study. *Phys. Rev. B* **1998**, *57*, 1505.

(34) Fung, V.; Tao, F. F.; en Jiang, D. Trends of Alkane Activation on Doped Cobalt (II, III) Oxide from First Principles. *Chem. Cat. Chem.* **2018**, *10*, 244–249.

(35) Liu, J.; Zhang, S.; Zhou, Y.; Fung, V.; Nguyen, L.; Jiang, D.; Shen, W.; Fan, J.; Tao, F. F. Tuning catalytic selectivity of oxidative catalysis through deposition of non-metallic atoms in surface lattice of metal oxide. *ACS Catal.* **2016**, *6*, 4218–4228.

(36) Rollmann, G.; Rohrbach, A.; Entel, P.; Hafner, J. First-principles calculation of the structure and magnetic phases of hematite. *Phys. Rev. B* **2004**, *69*, 165107.

(37) Aykol, M.; Wolverton, C. Local environment dependent GGA + U method for accurate thermochemistry of transition metal compounds. *Phys. Rev. B* **2014**, *90*, 115105.

(38) Eom, T.; Lim, H.-K.; Goddard, W. A.; Kim, H. First-Principles Study of Iron Oxide Polytypes: Comparison of GGA+U and Hybrid Functional Method. *J. Phys. Chem. C* **2015**, *119*, 556–562.

(39) Page, Y. L.; Saxe, P. Symmetry-general least-squares extraction of elastic data for strained materials from ab initio calculations of stress. *Phys. Rev. B* **2002**, *65*, 104104.

(40) Marmier, A.; Lethbridge, Z. A.; Walton, R. I.; Smith, C. W.; Parker, S. C.; Evans, K. E. ElAM: A computer program for the analysis and representation of anisotropic elastic properties. *Comput. Phys. Commun.* **2010**, *181*, 2102–2115.

(41) Maczka, M.; Pasinska, K.; Ptak, M.; Paraguassu, W.; da Silva, T. A.; Sieradzki, A.; Pikul, A. Effect of solvent, temperature and pressure on the stability of chiral and perovskite metal formate frameworks of $[NH_2NH_3][M(HCOO)_3]$ (M = Mn, Fe, Zn). *Phys. Chem. Chem. Phys.* **2016**, *18*, 31653–31663.

(42) Ghosh, P. S.; DeTellem, D.; Ren, J.; Witanachchi, S.; Ma, S.; Lisenkov, S.; Ponomareva, I. Unusual Properties of Hydrogen-Bonded Ferroelectrics: The Case of Cobalt Formate. *Phys. Rev. Lett.* **2022**, *128*, 077601.

(43) Ghosh, P. S.; Doherty, J.; Lisenkov, S.; Ponomareva, I. Tunability of Structure, Polarization, and Band Gap of High T_c Organic-Inorganic Ferroelectrics by Hydrostatic Pressure: First-Principles Study. *J. Phys. Chem. C* **2021**, *125*, 16296–16303.

(44) Stokes, H. T.; Hatch, D. M.; Campbell, B. J. ISOTROPY Software Suite, iso.byu.edu., 2015.

(45) Viswanathan, M. Structural Tunability Controlled by Uniaxial Strength in a Hybrid Perovskite. *J. Phys. Chem. C* **2019**, *123*, 6711–6716.

(46) Yang, Z.; Cai, G.; Bull, C. L.; Tucker, M. G.; Dove, M. T.; Friedrich, A.; Phillips, A. E. Hydrogen-bond-mediated structural variation of metal guanidinium formate hybrid perovskites under pressure. *Philos. Trans. Royal Soc. A PHILOS T R SOC A* **2019**, *377*, 20180227.

(47) Thomas, L. M.; Shanker, J. Equations of State and Pressure Dependence of Bulk Modulus for NaCl Crystals. *Phys. Status Solidi B* **1995**, *189*, 363–369.

(48) Jiang, X.; Yang, Y.; Molokeev, M.; Gong, P.; Liang, F.; Wang, S.; Liu, L.; Wu, X.; Li, X.; Li, Y. et al. Zero Linear Compressibility in Nondense Borates with a "Lu-Ban Stool"-Like Structure. *Adv. Mater.* **2018**, *30*, 1801313.

(49) Chung, H.-Y.; Weinberger, M. B.; Levine, J. B.; Kavner, A.; Yang, J.-M.; Tolbert, S. H.; Kaner, R. B. Synthesis of Ultra-Incompressible Superhard Rhenium Diboride at Ambient Pressure. *Science* **2007**, *316*, 436–439.

(50) Gui, D.; Ji, L.; Muhammad, A.; Li, W.; Cai, W.; Li, Y.; Li, X.; Wu, X.; Lu, P. Jahn-Teller Effect on Framework Flexibility of Hybrid Organic-Inorganic Perovskites. *J. Phys. Chem. Lett.* **2018**, *9*, 751–755.

(51) Ceperley, D. M.; Alder, B. J. Ground State of the Electron Gas by a Stochastic Method. *Phys. Rev. Lett.* **1980**, *45*, 566–569.

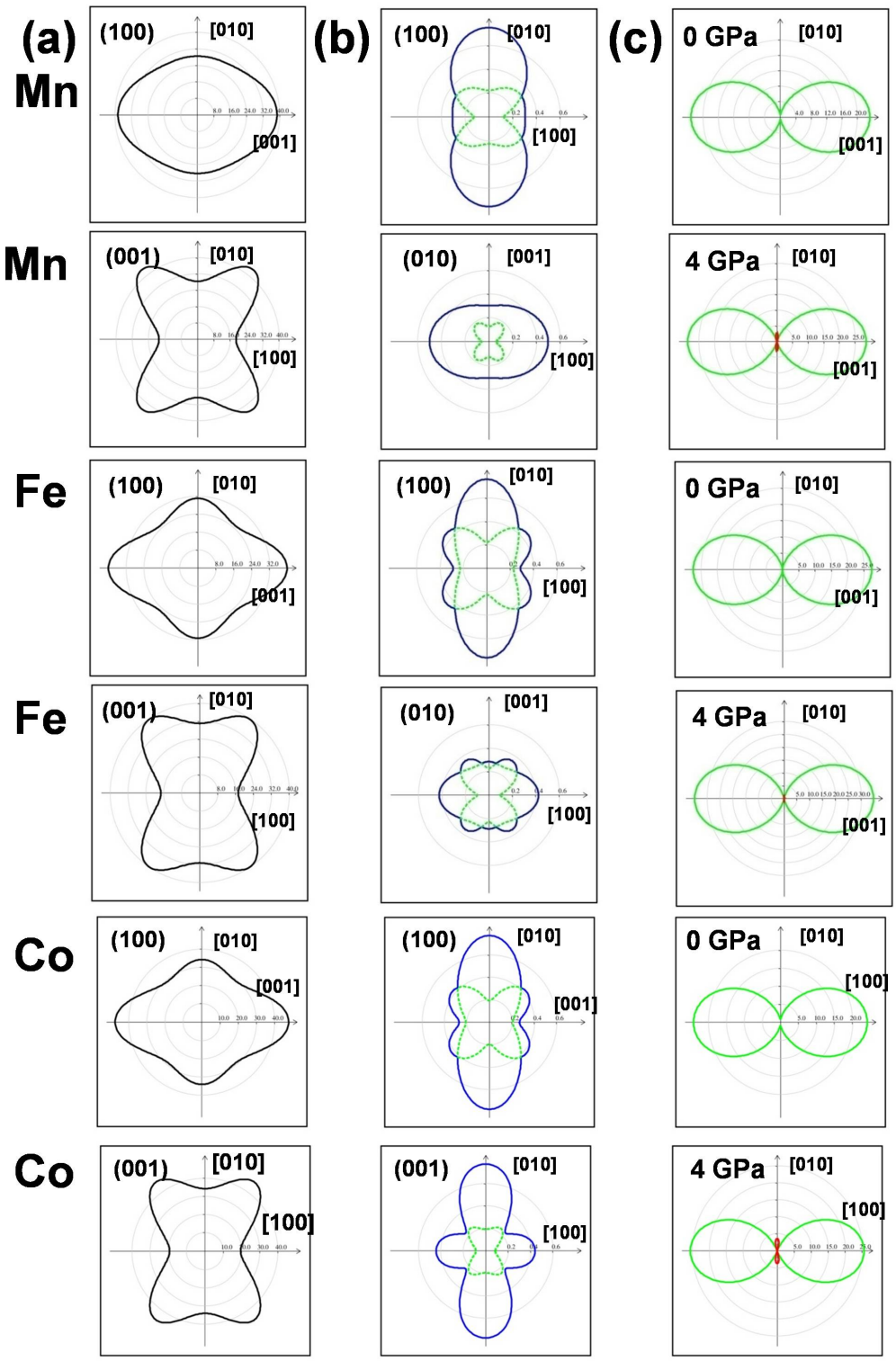

Figure 3: The 2D maps of Young's moduli (a), and Poisson ratios (b) at zero pressures for Mn-, Fe- and Co-HOIP; and linear compressibilities at 0 GPa and 4 GPa pressures for Mn-, Fe- and Co-HOIP (c). In (b) the blue outer line and green inner line show the maximum and minimum values, respectively. In (c) green line show the maximum values and red line shows negative values. The results of Co-HOIP are ploted from our previous study.[13]